Non-adiabatic couplings and conversion dynamics between localized and charge transfer excitations from Many-Body Green's Functions Theory

Gianluca Tirimbò[†] and Björn Baumeier[*,†]

[†]*Department of Mathematics and Computer Science, Eindhoven University of Technology, PO Box 513, 5600MB Eindhoven, the Netherlands*

[‡]*Institute for Complex Molecular Systems, Eindhoven University of Technology, PO Box 513, 5600MB Eindhoven, the Netherlands*

E-mail: b.baumeier@tue.nl

Abstract

We investigate the determination of non-adiabatic couplings between localized excitations (LEs) and charge-transfer (CT) excitations based on many-body Green's functions theory in the *GW* approximation with the Bethe–Salpeter equation (*GW*-BSE). Using a small molecule dimer system, we first study the influence of different diabatization methods, as well as different model choices within *GW*-BSE, such as the self-energy models or different levels of self-consistency, and find that these choices affect the LE-CT couplings only minimally. We then consider a large-scale low-donor morphology formed from rubrene and fullerene and evaluate the LE-CT couplings based on coupled *GW*-BSE-molecular mechanics calculations. For these disordered systems of bulky molecules, we observe differences in the couplings based on the Edmiston–Ruedenberg compared to the more approximate Generalize Mulliken–Hush and Fragment Charge Difference diabatization formalisms. In a kinetic model for the conversion between LE

and CT states, these differences affect the details of state populations in an intermediate timescale but not the final populations.

1 Introduction

Many photochemical processes, such as catalytic processes or the generation of charges in active layer heterostructures of organic solar cells, involve the transfer of an electron triggered by the absorption of a photon. Such photoinduced electron transfer reactions are typically influenced by a variety of properties, ranging from the intrinsic molecular electronic structure of the molecular building blocks of the material, the details of the local mutual arrangement of molecules, to larger scale morphological ordering. In many situations, the inherent disorder of the material systems in which the electron transfer takes place suggests the use of localized diabatic states to describe the reactions and to map the effects of the local and global environment onto them. This idea as given rise to multiscale simulation approaches, in which the transport of excitations across a material is modeled as a series of bi-molecular transfer events, each of them described by an effective transfer rate.[1–3] According to Marcus theory,[4,5] in the non-adiabatic high temperature or activated crossing limit, the rate of electronic excitation transfer between two states X (initial) and Y (final) is

$$\omega_{XY} = \frac{2\pi}{\hbar} \frac{|J_{XY}|^2}{\sqrt{4\pi\lambda_{XY} k_B T}} \exp\left[-\frac{(\Delta E_{XY} - \lambda_{XY})^2}{4\lambda_{XY} k_B T}\right], \tag{1}$$

where ΔE_{XY} is the free energy difference between initial and final states, and λ_{XY} the reorganization energy. The expression also contains the *non-adiabatic coupling* element, J_{XY}. In principle, it should be possible to evaluate all three quantities that enter the Marcus rate from electronic structure methods. To account for the local and global environment, however, it is typically required to embed electronic structure methods into a classical environment model,[6–8] as the size of realistic disordered systems at least on the order of several tens of nm exceeds the capabilities of explicit quantum chemistry methods. Besides such quantum-

classical embedding, of the key challenges involved in the multiscale modeling approaches of this kind is to use quantum-chemistry methods that allow for an accurate prediction of various excited states involved in the dynamical processes. Especially for the conversion of charge-neutral excitations, e.g., after photo absorption from localized exciton (LE) to charge-transfer (CT) state as an example of a photoinduced electron transfer reaction, the energetics of both LEs and CTs need to be described on an equal footing. In this context, the use of many-body Green's functions Theory employing the GW approximation and the Bethe–Salpeter equation (BSE)[9] has become attractive to model electronically excited states on top of a ground-state reference calculation typically performed on the level of density-functional theory (DFT).[10,11] It was shown that GW-BSE provides an effective single- and two-particle picture with accurate energies of LE and CT states without the need for any adaptations.[12–14] Previous work has also shown that the additional screening caused by the molecular environment strongly affects the energies (and also densities) of CT states,[15,16] more so than those of LEs, and that this energetic stabilization is important for finding CT-LE energy differences $\Delta E_{\text{LE-CT}}$ that are favorable for LE to CT conversion in organic solar cell materials. To fully treat the dynamical process of this conversion in the spirit of Eq. (1) requires also the reliable determination of the respective non-adiabatic coupling elements $J_{\text{LE-CT}}$.

In this work, we present a comparative study of determining non-adiabatic coupling elements between localized and charge-transfer excitations in the framework GW-BSE, based on three different diabatization methods: Edmiston–Ruedenberg (ER) diabatization[17] employing explicit electronic densities and the more approximate Generalize Mulliken–Hush (GMH)[18] and Fragment Charge Difference (FCD)[19] formalisms. We first validate the predicted $J_{\text{LE-CT}}$ in a small molecule dimer system consisting of naphthalene and tetracyanoethylene (TCNE), for which reference calculations from coupled-cluster and time-dependent density-functional theory are available[20] and allow scrutinizing the individual and combined effects of energy and (effective) wave-function predictions in the Green's functions method.

Herein, we also put particular emphasis on how much or little the different model choices within *GW*-BSE, such as the choice of self-energy models, different levels of self-consistency or the use of the Tamm–Dancoff approximation in the BSE, affect the LE-CT couplings.

To investigate how the findings for the ideal small-molecule dimer translate to larger-scale systems with potential relevance for materials applications, we proceed by applying different *GW*-BSE-based diabatization techniques to a mixed donor-acceptor blend of rubrene and fullerene.[21] Such a blend with low-donor content contains significantly larger molecules, exhibits substantial positional and orientational disorder, and allows therefore also a case study of the kinetics of the conversion from a photoexcited LE on rubrene to rubrene-fullerene CT states, typical intermediates for charge separation.

This paper is organized as follows: In Section 2, we provide a brief summary of the essentials of the *GW*-BSE method methodology, polarizable embedding approaches, as well as the three different diabatization methods used in this work. Results on the model naphthalene-TCNE dimer and the mixed donor-acceptor system of rubrene and fullerene are presented and discussed in Section 3. A short summary concludes the paper.

2 Methodology

Here, we briefly summarize the essentials of Many-Body Green's Functions Theory in the *GW* approximation with the BSE for the calculations of electronic excitations, its polarizable embedding, as well as the three diabatization methods we consider in this work.

2.1 Electronic Excitations via *GW*-BSE

In the framework of *GW*-BSE,[9,22] excitations are constructed based on a reference ground state calculation, here at the level of Kohn–Sham (KS) density-functional theory. One first

obtains KS wavefunctions $\phi_n^{\mathrm{KS}}(\mathbf{r})$ and energies $\varepsilon_n^{\mathrm{KS}}$ from

$$\left\{-\frac{\hbar^2}{2m}\nabla^2 + V_{\mathrm{ext}}(\mathbf{r}) + V_{\mathrm{H}}(\mathbf{r}) + V_{\mathrm{xc}}(\mathbf{r})\right\}\phi_n^{\mathrm{KS}}(\mathbf{r}) = \varepsilon_n^{\mathrm{KS}}\phi_n^{\mathrm{KS}}(\mathbf{r}). \tag{2}$$

Here, V_{ext} is the external potential, V_{H} the Hartree potential, and V_{xc} the exchange-correlation potential. Hedin[23,24] introduced the GW approximation of many-body Green's functions theory, in which quasi-particle (QP) states representing independent electron and hole excitations are found as solutions the quasi-particle equations:

$$\left\{-\frac{\hbar^2}{2m}\nabla^2 + V_{\mathrm{ext}}(\mathbf{r}) + V_{\mathrm{H}}(\mathbf{r})\right\}\phi_n^{\mathrm{QP}}(\mathbf{r}) + \int \Sigma(\mathbf{r},\mathbf{r}',\varepsilon_n^{\mathrm{QP}})\phi_n^{\mathrm{QP}}(\mathbf{r}')d\mathbf{r}' = \varepsilon_n^{\mathrm{QP}}\phi_n^{\mathrm{QP}}(\mathbf{r}). \tag{3}$$

In place of the exchange-correlation potential in Eq. (2), the energy-dependent self-energy operator $\Sigma(\mathbf{r},\mathbf{r}',E)$ occurs in the QP equations. This operator is evaluated using the one-body Green's function in quasi-particle approximation

$$G(\mathbf{r},\mathbf{r}',\omega) = \sum_n \frac{\psi_n(\mathbf{r})\psi_n^*(\mathbf{r}')}{\omega - \varepsilon_n + i0^+\mathrm{sgn}(\varepsilon_n - \mu)} \tag{4}$$

as

$$\Sigma(\mathbf{r},\mathbf{r}',E) = \frac{i}{2\pi}\int e^{-i\omega 0^+} G(\mathbf{r},\mathbf{r}',E-\omega)W(\mathbf{r},\mathbf{r}',\omega)\,d\omega, \tag{5}$$

where W denotes the dynamically screened Coulomb interaction. This is determined by first computing the polarization P in the random-phase approximation (RPA),[25,26] then with it the microscopic dielectric function as a convoluting of P with the bare Coulomb interaction v, i.e., $\epsilon = 1 - vP$. Finally, W is obtained as $W = \epsilon^{-1}v$, i.e., after inversion of ϵ and subsequent convolution with the bare Coulomb interaction. The frequency integration in Eq. (5) can be performed fully analytically (FA) based on contour deformation techniques or with the use of a generalized plasmon-pole model (PPM),[27] which extends the RPA result for $\omega = 0$ (static polarization) and the associated static dielectric function to the dynamic one.

Assuming that $|\phi_n^{\mathrm{QP}}\rangle \approx |\phi_n^{\mathrm{KS}}\rangle$, the quasiparticle energies can be evaluated perturbatively

according to

$$\varepsilon_n^{\mathrm{QP}} = \varepsilon_n^{\mathrm{KS}} + \Delta\varepsilon_n^{GW} = \varepsilon_n^{\mathrm{KS}} + \langle\phi_n^{\mathrm{KS}}|\widehat{\Sigma}(\varepsilon_n^{\mathrm{QP}}) - \widehat{V}_{\mathrm{xc}}|\phi_n^{\mathrm{KS}}\rangle. \tag{6}$$

As the correction $\Delta\varepsilon_n^{GW}$ itself depends on $\varepsilon_n^{\mathrm{QP}}$, Eq. (6) needs to be solved self-consistently. In the G_0W_0 approximation, the single-particle energies that enter the RPA calculation of ϵ^{-1} and G are the $\varepsilon_n^{\mathrm{KS}}$. Updating these energies self-consistently with the corrections from Eq. (6) leads to the so-called eigenvalue self-consistent evGW variant.

Neutral excitations with a conserved number of electrons can be obtained from the Bethe–Salpeter Equation (BSE).[24,28] It determines the four-point density response function of the interacting system from the non-interacting system.[7,9,29] Coupled electron-hole amplitudes of excitation S can be expressed in a product basis of QP wave functions, i.e.,

$$\chi_S(\mathbf{r}_{\mathrm{e}}, \mathbf{r}_{\mathrm{h}}) = \sum_{v}^{\mathrm{occ}} \sum_{c}^{\mathrm{unocc}} A_{vc}^S \phi_c(\mathbf{r}_{\mathrm{e}})\phi_v^*(\mathbf{r}_{\mathrm{h}}) + B_{vc}^S \phi_v(\mathbf{r}_{\mathrm{e}})\phi_c^*(\mathbf{r}_{\mathrm{h}}), \tag{7}$$

where $\mathbf{r}_{\mathrm{e}}$ ($\mathbf{r}_{\mathrm{h}}$) is for the electron (hole) coordinate, and we drop the label QP for clarity. Here, A_{vc} (B_{vc}) are the expansion coefficients of the excited state wave function in terms of resonant (anti-resonant) transitions between QP occupied (occ.) states v and unoccupied (unocc.) c, respectively. In this basis, the BSE turns into an effective two-particle Hamiltonian problem of the form

$$\begin{pmatrix} \underline{\mathbf{H}}^{\mathrm{res}} & \underline{\mathbf{K}} \\ -\underline{\mathbf{K}} & -\underline{\mathbf{H}}^{\mathrm{res}} \end{pmatrix} \begin{pmatrix} \mathbf{A}^S \\ \mathbf{B}^S \end{pmatrix} = \Omega_S \begin{pmatrix} \mathbf{A}^S \\ \mathbf{B}^S \end{pmatrix}. \tag{8}$$

Specifically for singlet excitations, the matrix elements of the blocks $\underline{\mathbf{H}}^{\mathrm{res}}$ and $\underline{\mathbf{K}}$ are calculated as

$$H_{vc,v'c'}^{\mathrm{res}} = D_{vc,v'c'} + 2K_{vc,v'c'}^{\mathrm{x}} + K_{vc,v'c'}^{\mathrm{d}} \tag{9}$$

$$K_{cv,v'c'} = 2K_{cv,v'c'}^{\mathrm{x}} + K_{cv,v'c'}^{\mathrm{d}}\,, \tag{10}$$

with

$$D_{vc,v'c'} = (\varepsilon_c - \varepsilon_v)\delta_{vv'}\delta_{cc'}, \tag{11}$$

$$K^{\mathrm{x}}_{vc,v'c'} = \int \mathrm{d}^3\mathbf{r}_\mathrm{e}\,\mathrm{d}^3\mathbf{r}_\mathrm{h}\,\phi^*_c(\mathbf{r}_\mathrm{e})\phi_v(\mathbf{r}_\mathrm{e})v_\mathrm{C}(\mathbf{r}_\mathrm{e},\mathbf{r}_\mathrm{h})\phi_{c'}(\mathbf{r}_\mathrm{h})\phi^*_{v'}(\mathbf{r}_\mathrm{h}) \tag{12}$$

$$K^{\mathrm{d}}_{vc,v'c'} = -\int \mathrm{d}^3\mathbf{r}_\mathrm{e}\,\mathrm{d}^3\mathbf{r}_\mathrm{h}\,\phi^*_c(\mathbf{r}_\mathrm{e})\phi_{c'}(\mathbf{r}_\mathrm{e})W(\mathbf{r}_\mathrm{e},\mathbf{r}_\mathrm{h},\omega=0)\phi_v(\mathbf{r}_\mathrm{h})\phi^*_{v'}(\mathbf{r}_\mathrm{h})\,. \tag{13}$$

Here, K^{x} is the repulsive exchange interaction originating from the bare Coulomb term v_C, while the direct interaction K^{d} contains the attractive, but screened, interaction W between electron and hole, causing the binding of the electron-hole pair. In Eq. (13) it is assumed that the dynamic properties of $W(\omega)$ are negligible, and the computationally less demanding static approximation $\omega = 0$ is employed. If off-diagonal blocks $\underline{\mathbf{K}}$ in Eq. (8) are small, the additional use of the Tamm–Dancoff Approximation (TDA)[30] is convenient, in which the electron-hole amplitude is expressed only as resonant transitions from occupied v to unoccupied c states:

$$\chi_S^{\mathrm{TDA}}(\mathbf{r}_\mathrm{e},\mathbf{r}_\mathrm{h}) = \sum_v^{\mathrm{occ}}\sum_c^{\mathrm{unocc}} A^S_{\mathrm{TDA},vc}\phi_c(\mathbf{r}_\mathrm{e})\phi^*_v(\mathbf{r}_\mathrm{h}), \tag{14}$$

thereby reducing the effective Hamiltonian tothe upper diagonal block of Eq. (8):

$$\underline{\mathbf{H}}^{\mathrm{res}}\mathbf{A}^S_{\mathrm{TDA}} = \Omega^{\mathrm{TDA}}_S\mathbf{A}^S_{\mathrm{TDA}}. \tag{15}$$

For all practical GW-BSE calculations in this work, we use the Gaussian-type orbitals implementations in the VOTCA-XTP[7,8] software.

2.2 Polarizable Embedding

To account for effects of electronic excitations in complex molecular environment, a quantum (QM) region with the excited state complex is embedded in a classical, polarizable atomistic

(MM) model for the environment. The QM/MM scheme in VOTCA-XTP makes use of a distributed atomic multipole representation for molecules in the MM region, which allows treatment of both the effects of static electric fields and the polarization response as a self-consistent reaction field. Specifically, this classical MM energy for the system is evaluated as

$$E_{\mathrm{MM}} = \frac{1}{2} \sum_{\substack{A,B \\ A \neq B}} \sum_{a \in A} \sum_{b \in B} \sum_{tu} (Q_t^a + \Delta Q_t^a) T_{tu}^{ab} Q_u^b, \tag{16}$$

where A and B indicate individual molecules in the system, a and b atoms in the respective molecules, Q_t^a are the static atomic multipole moments of rank t associated to atom a, and T_{tu}^{ab} is the tensor describing the interactions between the multipoles moments Q_t^a and Q_u^b.[31] The induced moments ΔQ_t^a are generated by the electric field created by moments t' of atom $a' \neq a$ in molecule A and the one generated by the moment u of atom b in molecule B:

$$\Delta Q_t^a = - \sum_{\substack{A,B \in \mathcal{S} \\ A \neq B}} \sum_{b \in B} \sum_{\substack{a' \in A \\ a' \neq a}} \sum_{tt'u} \alpha_{tt'}^{aa'} T_{t'u}^{a'b} (Q_u^b + \Delta Q_u^b), \tag{17}$$

with $\alpha_{tt'}^{aa'}$ the atomic polarizability on each site. To avoid effects of spurious overpolarization, a damped version of the interaction tensor (Thole damping[31]) is used. Then, the static and induced multipoles in the MM region also interact with the electron density in QM region via an additional external potential to Eq. (2). At the same time, the explicit electrostatic field from the QM density is included in polarizing the MM region. The total density of excited state S is evaluated from the excited-state wavefunction χ^S as

$$\rho^S(\mathbf{r}) = \rho_{\mathrm{DFT}}(\mathbf{r}) + \rho_e^S(\mathbf{r}) - \rho_h^S(\mathbf{r}), \tag{18}$$

with

$$\rho_{\mathrm{e}}^{S}(\mathbf{r}) = \rho_{\mathrm{e}}^{S}(\mathbf{r}_{\mathrm{e}}) = \int d\mathbf{r}_{\mathrm{h}} |\chi_S(\mathbf{r}_{\mathrm{e}}, \mathbf{r}_{\mathrm{h}})|^2$$
$$\rho_{\mathrm{h}}^{S}(\mathbf{r}) = \rho_{\mathrm{h}}^{S}(\mathbf{r}_{\mathrm{h}}) = \int d\mathbf{r}_{\mathrm{e}} |\chi_S(\mathbf{r}_{\mathrm{e}}, \mathbf{r}_{\mathrm{h}})|^2. \tag{19}$$

In order to obtain the polarization response of both the QM and MM regions, a self-consistent procedure is employed. At step p of this procedure, the total energy of the coupled QM/MM system for the state S of interest (ground state $S = 0$, or excited states $S > 0$) is determined as

$$E_{\mathrm{QM/MM}}^{S,p} = E_{\mathrm{QM}}^{S,p} + E_{\mathrm{MM}}^{S,p}, \tag{20}$$

with

$$E_{\mathrm{QM}}^{S,p} = E_{\mathrm{DFT}}^{S,p} + \Omega_S^p, \tag{21}$$

and $\Omega_S^p = 0$ for the ground state case. The whole procedure is repeated until the change of total energy is less than a preselected accuracy, typically 10^{-5} Ha. The excitation energy $\Omega_S^{\mathrm{QM/MM}}$ of a complex in the polarizable environment is then obtained as the difference

$$\Omega_S^{\mathrm{QM/MM}} = E_{\mathrm{QM/MM}}^{S} - E_{\mathrm{QM/MM}}^{0}. \tag{22}$$

2.3 Diabatization Methods

Electronic states obtained from as eigenstates of some (approximate) Hamiltonian are adiabatic states $|\Phi_i\rangle$, such as the excitations χ_S obtained from the BSE as introduced in Section 2.1. Corresponding diabatic states $|\Phi_a^{\mathrm{diabatic}}\rangle$, needed for the evaluation and understanding of electron transfer processes, can be found via a unitary transformation

$$|\Phi_a^{\mathrm{diabatic}}\rangle = \sum_{j=1}^{N_{\mathrm{states}}} U_{aj} |\Phi_j\rangle. \tag{23}$$

The unitary transformation matrix $\underline{\mathbf{U}}$ is determined by extremalizing some function $f(\underline{\mathbf{U}})$, and various methods differ by the definition of this function, with some choices being discussed below. With this, the adiabatic form of the electronic Hamiltonian $\mathrm{H_{el}}$ with adiabatic energies ε_i, i.e., $\langle\Phi_i|\mathrm{H_{el}}|\Phi_j\rangle = \varepsilon_j\delta_{ij}$ is transformed into the diabatic form

$$H_{ab}^{\text{diabatic}} = \langle\Phi_a^{\text{diabatic}}|\mathrm{H_{el}}|\Phi_b^{\text{diabatic}}\rangle = \sum_{ij} U_{ia}\langle\Phi_i|\mathrm{H_{el}}|\Phi_j\rangle U_{bj}. \tag{24}$$

For the two-state problem ($N_{\text{states}} = 2$), the transformation can be written explicitly as a rotation

$$\underline{\mathbf{U}} = \begin{pmatrix} U_{11} & U_{12} \\ U_{21} & U_{22} \end{pmatrix} = \begin{pmatrix} \cos\theta & -\sin\theta \\ \sin\theta & \cos\theta \end{pmatrix}. \tag{25}$$

and the diabatic Hamiltonian as

$$\underline{\mathbf{H}}^{\text{diabatic}} = \begin{pmatrix} \cos\theta & \sin\theta \\ -\sin\theta & \cos\theta \end{pmatrix} \begin{pmatrix} \varepsilon_1 & 0 \\ 0 & \varepsilon_2 \end{pmatrix} \begin{pmatrix} \cos\theta & -\sin\theta \\ \sin\theta & \cos\theta \end{pmatrix}. \tag{26}$$

Its off-diagonal elements

$$J_{ab}^{\text{ER}} = \frac{1}{2}\sin(2\theta)(\varepsilon_2 - \varepsilon_1) \tag{27}$$

are then the non-adiabatic couplings between the two diabtic states.

2.3.1 Edmiston-Ruedenberg Diabatization

In the Edmiston-Ruedenberg (ER) localized diabatization formalism,[32] the objective is the maximization of the self-repulsion of the diabats via

$$f_{\text{ER}}(U) = \sum_{i,j,k,l,m} U_{ji}U_{ki}U_{li}U_{mi}R_{jklm}. \tag{28}$$

Here, the tensor R_{jklm} is defined in basis of molecular orbitals as

$$R_{jklm} = \sum_{vcv'c'} D^{jk}_{vc}(vc|v'c')D^{lm}_{v'c'}. \tag{29}$$

with

$$(vc|v'c') = \iint \frac{\phi_v(\mathbf{r})\phi_c(\mathbf{r})\phi_{v'}(\mathbf{r}')\phi_{c'}(\mathbf{r}')}{|\mathbf{r}-\mathbf{r}'|} d\mathbf{r}\, d\mathbf{r}', \tag{30}$$

where the indices v, v' and c, c' spanning the occupied and unoccupied levels, respectively. In Eq. 29, $\underline{\mathbf{D}}^{jk}$ is the excited state transition density matrix between the excited states j and k. If the $\phi_n(\mathbf{r})$ are expressed in an atomic orbital basis $\{\chi_\alpha(\mathbf{r})\}$ according to $\phi_n(\mathbf{r}) = \sum_\alpha d^n_\alpha \chi_\alpha(\mathbf{r})$, Eq. (29) can be rewritten as

$$R_{jklm} = \sum_{\alpha\beta\gamma\delta} D^{jk}_{\alpha\beta}(\alpha\,\beta|\gamma\,\delta)D^{lm}_{\gamma\delta}. \tag{31}$$

The tensor $(\alpha\,\beta|\gamma\,\delta)$ is part of the standard implementation of DFT-GW-BSE, in which the transition density matrix between states j and k in the atomic orbital basis reads

$$D^{jk}_{\alpha\beta} = D^0_{\alpha\beta}\delta_{jk} + \sum_{cc'} d^c_\alpha M^{jk}_{cc'} d^{c'}_\beta - \sum_{vv'} d^v_\alpha M^{jk}_{vv'}, d^{v'}_\beta \tag{32}$$

where

$$M^{jk}_{cc'} = \sum_v \left(A^j_{vc}A^k_{vc'} - B^j_{vc}B^k_{vc'}\right) \tag{33}$$

and

$$M^{jk}_{vv'} = \sum_c \left(A^j_{vc}A^k_{v'c} - B^j_{vc}B^k_{v'c}\right). \tag{34}$$

With these definitions, Eq. (31) can be computed and the ER functional can be maximized. For the two-state case, there is a closed form for this maximizing angle.[17] It is

computed with the help of

$$A_{12} = R_{1212} - \frac{1}{4}\big(R_{1111} + R_{2222} - 2\,R_{1122}\big) \tag{35}$$

$$B_{12} = R_{1112} - R_{2212} \tag{36}$$

as

$$\cos(4\theta) = -\frac{A_{12}}{\sqrt{A_{12}^2 + B_{12}^2}}. \tag{37}$$

2.3.2 Generalized Mulliken–Hush Diabatization

In the Generalized Mulliken–Hush (GMH) approach to diabatization,[18,33] the adabatic-to-diabatic transformation is based on the definition of the diabatic states as eigenstates of the dipole moment. Specifically in a two-state model, the method requires the calculation of the dipole moment of each adiabatic state $\boldsymbol{\mu}_1$ and $\boldsymbol{\mu}_1$, and the transition dipole moment between the two, $\boldsymbol{\mu}_{12}$. The non-adabatic coupling element is then calculated as

$$J_{ab}^{\mathrm{GMH}} = \frac{|\hat{\mu}_{12}|(\varepsilon_2 - \varepsilon_1)}{((\boldsymbol{\mu}_1 - \boldsymbol{\mu}_2)^2 + 4\hat{\mu}_{12}^2)^{1/2}}, \tag{38}$$

where $\hat{\mu}_{12}$ is the projection of $\boldsymbol{\mu}_{12}$ on the charge transfer direction $(\boldsymbol{\mu}_1 - \boldsymbol{\mu}_2)/|\boldsymbol{\mu}_1 - \boldsymbol{\mu}_2|$.

2.3.3 Fragment Charge Difference Diabatization

Another alternative is to determine the diabatic states as eigenstates of the so-called fragment charge difference (FCD) matrix,[19] based on the definition of donor (D) and acceptor (A) fragments, as $\Delta Q_{ij} = Q_{ij}(D) - Q_{ij}(A)$. The fragment charges are typically obtained from a population analysis of the individual adiabatic densities and the transition density between them. Again, for a two-state model, the coupling is given by

$$J_{ab}^{\mathrm{FCD}} = \frac{|\Delta Q_{12}|(\varepsilon_2 - \varepsilon_1)}{((\Delta Q_{11} - \Delta Q_{22})^2 + 4\Delta Q_{12}^2)^{1/2}}. \tag{39}$$

3 Results

3.1 Naphthalene-TCNE complex

Stacked geometries of naphthalene and TCNE with different intermolecular distances are taken from Ref.[20] Ground state calculations on KS-DFT level are performed with the ORCA[34] package using both the PBE0 functional[35] and the def2-tzvp basis[36] together with optimized auxiliary basis sets[37] in resolution-of-identity techniques to efficiently express terms involving four-center Coulomb integrals. We compare in the following the results based on G_0W_0 calculations and eigenvalue selfconsistent evGW calculations. The convergence limit for the self-consistent GW-cycles in the evGW scheme was set to 10^{-5} Hartree (0.27 meV). Quasiparticle corrections are determined for the 197 lowest energy orbitals, and the product basis for the electron-hole wavefunctions are formed from the 66 occupied and 131 lowest unoccupied orbitals. All orbitals are included in the RPA step for calculating the dielectric function, i.e., 320 orbitals for def2-svp, 668 for def2-tzvp, and 1380 for def2-qzvp, respectively. Both, the fully analytic approach (FAA) and a generalized plasmon-pole model as introduced in Section 2.1 as used for the frequency integration of the self-energy. The obtained excitation energies for all variants are summarized in Tab. 1.

In Fig. 1(a), we show the distance-dependent LE-CT couplings as resulting from evGW-BSE calculations with the FAA, the def2-tzvp basis set, and PBE0 in the ground state calculation. We first compare the influence of the choice of diabatization method, with the couplings obtained from ER shown as circles, from GMH as crosses, and FCD as diamonds, respectively. While both GMH and FCD methods appear to yield very similar couplings with a maximum deviation of 4 meV at a separation of 3.5 Å (see also Tab. 2), the $J^{\mathrm{ER}}_{\mathrm{LE\text{-}CT}}$ result slightly lower, e.g., by 9 meV at the closest distance. Note that the respective slopes of the three GW-BSE based data are identical, reflecting the same exponential decay of the LE-CT coupling with distance. Comparing out results to those obtained by EOM-EE-CCSD/GMH and TDDFT/FCD with the ωB97X-D[38] functional[20] shown in Fig. 1(a) as solid and dashed

Table 1: Distance-dependence of the low-energy LE and CT excitation energies (in eV) in a naphthalene-TCNE complex, based on different variants of GW-BSE using the def2-tzvp basis set and the PBE0 functional in the DFT ground state calculation.

	FAA				PPM			
	evGW		G_0W_0		evGW		G_0W_0	
	full	TDA	full	TDA	full	TDA	full	TDA
LE energy								
3.5 Å	4.309	4.341	3.998	4.022	4.255	4.262	4.006	4.035
3.9 Å	4.306	4.340	4.000	4.024	4.266	4.306	4.007	4.037
4.0 Å	4.306	4.339	4.000	4.024	4.264	4.305	4.006	4.036
4.5 Å	4.305	4.339	3.997	4.022	4.262	4.303	4.003	4.033
5.0 Å	4.300	4.333	3.995	4.020	4.257	4.299	4.000	4.030
CT energy								
3.5 Å	2.214	2.220	1.875	1.880	2.255	2.261	1.976	1.982
3.9 Å	2.387	2.389	2.052	2.054	2.430	2.432	2.157	2.159
4.0 Å	2.424	2.426	2.090	2.092	2.467	2.469	2.195	2.197
4.5 Å	2.589	2.590	2.255	2.255	2.632	2.632	2.360	2.361
5.0 Å	2.727	2.727	2.396	2.396	2.770	2.770	2.501	2.501
LE-CT difference								
3.5 Å	2.095	2.121	2.123	2.141	2.000	2.001	2.030	2.053
3.9 Å	1.920	1.951	1.948	1.970	1.836	1.874	1.850	1.878
4.0 Å	1.881	1.913	1.909	1.932	1.797	1.836	1.811	1.839
4.5 Å	1.716	1.749	1.743	1.767	1.630	1.670	1.642	1.673
5.0 Å	1.572	1.606	1.599	1.623	1.488	1.529	1.499	1.529

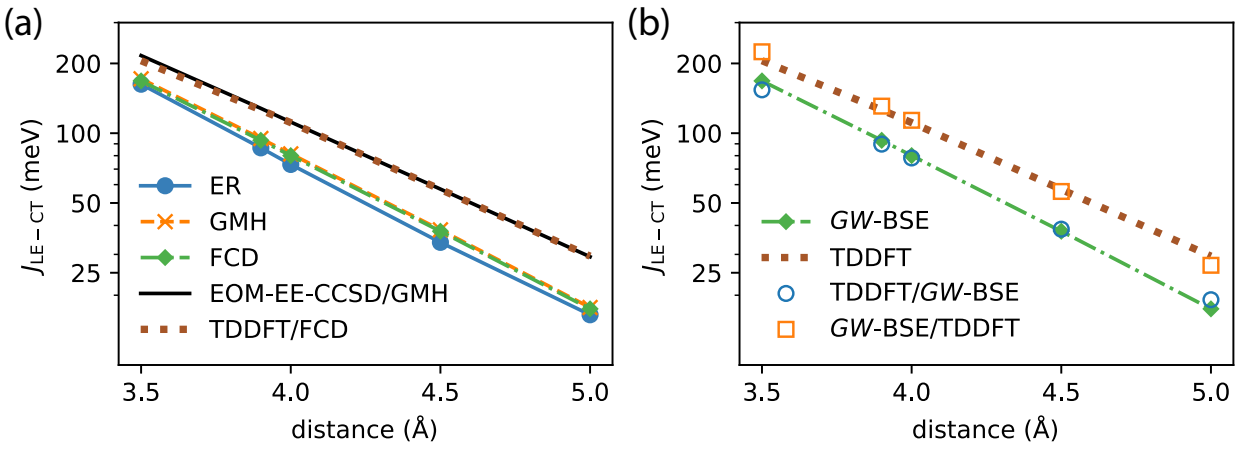

Figure 1: Distance dependence of LE-CT coupling elements in the naphthalene-TCNE complex. (a) *GW*-BSE results with the ER, GHM, and FCD diabatization methods based on full BSE solutions following ev*GW* calculations with FAA frequency integration, employing the def-tzvp basis and PBE0 functional in the ground state DFT run. Reference results on EOM-EE-CCSD and TDDFT levels are taken from Ref.[20] (b) Pure *GW*-BSE and TDDFT results based on FCD as in (a) compared to mixed methods, in which the fragment charge factor is taken from TDDFT and the energy difference from *GW*-BSE (TDDFT/*GW*-BSE) and vice-versa, showing that the difference between the pure *GW*-BSE and TDDFT results originate from the different predicted energies.

lines, respectively, we observe a combination of an offset to lower energies and a slightly stronger slope in *GW*-BSE. For instance, at the optimal intermolecular distance of 3.9 Å, EOM-EE-CSSD/GMH predicts a LE-CT coupling of 128 meV, TDDFT/FCD 126 meV, compared to 86 meV from ER, 95 meV from GMH, and 93 meV from FCD with *GW*-BSE. To understand this difference, we take a closer look at the results obtained with FCD diabatization in Fig. 1(b). The *GW*-BSE and TDDFT results are from Fig. 1(a) are shown again, now combined with "mixed" versions. In these versions, we first distinguish in the expression for $J^{\mathrm{FCD}}_{\mathrm{LE\text{-}CT}}$ between the fragment charge contribution $f_{\mathrm{FCD}} = J^{\mathrm{FCD}}_{\mathrm{LE\text{-}CT}}/(\varepsilon_2 - \varepsilon_1)$ and the energy contribution $f_\varepsilon = (\varepsilon_2 - \varepsilon_1)$. Then we combine f_{FCD}(TDDFT) with f_ε(*GW*-BSE) (TDDFT/*GW*-BSE) and vice versa (*GW*-BSE/TDDFT). For the former, we find that the resulting couplings are essentially identical to the ones from pure *GW*-BSE, while the latter results are in close agreement with the full pure TDDFT data. This corroborates the notion that the difference between the pure TDDFT and *GW*-BSE derived couplings can to

a large extend be attributed to differences in the energies. From Tab. 1, the LE-CT energy difference at the optimal naphthalene TCNE distance is 1.92 eV in GW-BSE and 2.70 eV in TDDFT,[20] and their ratio almost exactly translates into the ratio of the respective coupling elements.

Table 2: LE-CT coupling elements (in meV) in the naphthalene-TCNE complex at several intermolecular distances, as obatined using ER, GMH, and FCD diabatization with different variants of GW-BSE using the def2-tzvp basis set and the PBE0 functional in the DFT ground state calculation.

	FAA				PPM			
	evGW		G_0W_0		evGW		G_0W_0	
	full	TDA	full	TDA	full	TDA	full	TDA
ER diabatization								
3.5 Å	163	165	158	161	161	163	155	155
3.9 Å	86	87	84	85	88	89	86	86
4.0 Å	73	74	71	72	75	76	73	73
4.5 Å	34	34	33	33	35	35	34	34
5.0 Å	16	17	16	17	17	18	17	17
GMH diabatization								
3.5 Å	172	172	169	169	169	169	165	165
3.9 Å	95	95	93	94	93	93	92	92
4.0 Å	81	81	80	80	80	80	79	79
4.5 Å	38	38	38	38	38	38	37	37
5.0 Å	18	18	18	18	17	17	17	17
FCD diabatization								
3.5 Å	168	168	165	166	165	165	161	162
3.9 Å	93	93	92	92	92	92	90	90
4.0 Å	80	80	79	80	79	79	77	77
4.5 Å	38	38	37	37	37	37	37	37
5.0 Å	17	17	17	17	17	17	17	17

Table 2 also contains LE-CT couplings as obtained from different variants of GW-BSE, in which we have changed the exact frequency integration in Eq. (5) with a PPM, the level of GW from evGW to G_0W_0, and/or the BSE from its full form to the TDA. Overall, the $J_{\text{LE-CT}}$ are not very sensitive to the specific choices in the GW and BSE steps. For the sake of clarity, we will focus on the results from ER diabatization at the optimal separation of 3.9 Å in the following. First, the use of the TDA of the BSE impacts the couplings by only 1 meV, also

the use of the one-shot G_0W_0 method instead on evGW does not show differences exceeding 3 meV. Even the use of the PPM in place of the exact frequency integration (FAA) is of the same order, so that all values are within 3 % of the FAA/evGW/full BSE result. Similar observations also hold for the other intermolecular distances and diabatization techniques.

3.2 Rubrene-fullerene low-donor content system

We now move from the well-ordererd, small molecule naphthalene-TCNE dimer to a disordered cluster of larger molecules and investigate the sensitivity of LE-CT coupling elements based on GW-BSE on the different diabatization methods and if eventual differences propagate to different answers in dynamic models of conversion between LE and CT states. Specifically, we study an amorphous morphology with low-donor content (< 10 mol%), composed of fullerene (C_{60}) and 5,6,11,12-tetraphenyltetracene (rubrene).[21] Because of the low-donor content, a C_{60} cluster will surround the donor molecule, making the interaction between the single donor molecule with a close shell of neighboring C_{60} acceptors representative of the properties of the system as a whole. These complexes are therefore meaningful candidates for a computational analysis of the influence of donor-acceptor conformations and environment polarization effects in the GW-BSE/MM framework introduced in Sec. 2.2 and its consequence on the conversion dynamics between initially excited LE on rubrene (LE_R) to CT excitations.

3.2.1 CT density of states

To obtain representative structures, mixed morphologies have been simulated with ab-initio MD based on Density Functional Tight Binding theory using linear scaling self-consistent field calculations within the CP2K code.[39] Initial configurations have been prepared using Packmol,[40] targeting experimental values[21] for densities and mole percentages. This structure is first equilibrated at 700 K in NpT (with velocity rescaling thermostat[41] at atmospheric pressure[42]) for 7 ps (time step 1 fs), then annealed to 300 K within 10 ps. A final

NpT equilibration followed for 5 ps.

For calculating the LE and CT densities of states, C_{60} molecules are selected which are approximately in the first neighbor shell around one rubrene molecule. Given the conformation of this low-donor content materials, the behavior of this shell of molecules should be representative of the overall behavior of the material. After selection, polarizable GW-BSE/MM embedding calculations as described in Section 2.2 are performed for all dimers formed by rubrene and fullerene. Specifically, we employ for the GW-BSE calculations the def2-tzvp basis set[36] with an optimized auxiliary basis[37] for the steps including resolution-of-identity. The ground-state DFT calculation uses the PBE0 functional.[35] Eigenvalue self-consistent GW (evGW) calculations are performed to obtain the explicit quasiparticle-corrected energies for the highest 100 occupied and lowest 100 unoccupied orbitals, respectively. All orbitals are included in the RPA step and not explicitly GW corrected levels are scissors shifted according to the highest absolute quasiparticle correction among the explicitly corrected occupied or unoccupied orbitals, respectively. The frequency integration in Eq. (5) is performed using the PPM. Coupled electron-hole wavefunctions according to Eq. (7) are constructed using transitions between the highest 220 occupied and 220 lowest unoccupied states. In the MM part of the GW-BSE/MM, polarizable electrostatic interactions are taken into account within a cutoff of 4 nm.

The resulting energies of CT and LE excitations are depicted in Fig. 2. In general, the effects of polarizable embedding on the LE energies are small, as has been observed before, e.g., for embedded push-pull polymers[15] or small-molecule donor molecules.[8] Therefore, we only show the GW-BSE/MM results for the respective LEs, indicated by the blue (rubrene at 2.01 eV) and orange (C_{60} at 1.97 eV) vertical lines as there is no noticeable disorder. For the CT excitations, the GW-BSE calculations in vacuum already reveal significant energetic disorder, originating from the different rubrene-C_{60} conformations and the long-range electrostatic interaction between electron and hole. Individual CT excitation energies are marked by the short green vertical lines in Fig. 2, where we also show a density-of-states

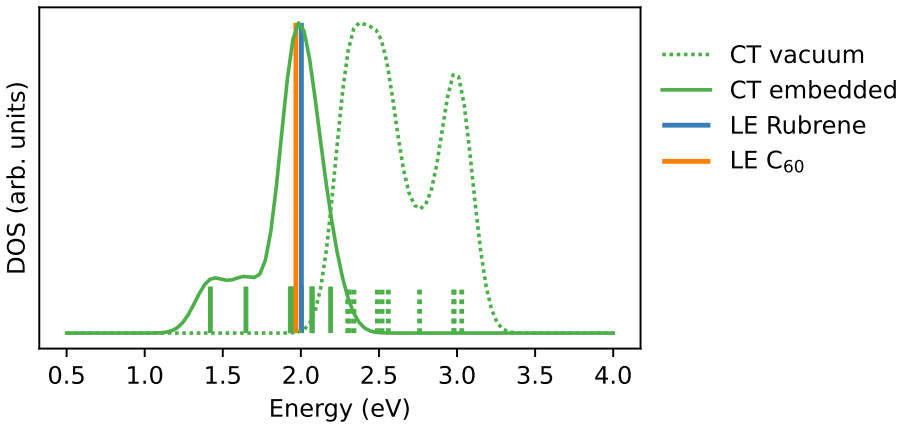

Figure 2: Energies of CT excitations (green vertical bars) from vacuum *GW*-BSE (dashed) and *GW*-BSE/MM calculations with polarizable embedding (solid). Solid and dashed curves indicate respective density-of-states obtained by Gaussian broadening with 0.1 eV as a guide-to-the-eye. Blue and orange lines highlight the *GW*-BSE/MM energies of LEs on rubrene and C_{60}, respectively.

obtained by broadening with a Gaussian function of width 0.1 eV. After polarizable embedding in *GW*-BSE/MM the CT energies (solid green lines) are shifted to lower energies, with energetic stabilization of up to 1 eV. Note that in vacuum, the CT excitation energies result generally higher than both LEs, which would make a conversion process of a LE on rubrene to a CT state energetically unlikely. After embedding, we find that the energetic stabilization brings several high-energy CTs close to the LEs, and some notably very much lower at 1.65 eV (CT_1)and 1.42 eV (CT_0), respectively. The latter compares favorably with the experimentally measured CT energy of 1.46 eV reported in Ref.[21] However, given the disorder in the CT excitation energies, it is unclear if the measurement truly probes simply the lowest-energy CT state, or one that is preferably dynamically populated during the timescale of the conversion process and the experiment.

3.2.2 Non-adiabatic LE-CT couplings

To proceed beyond considering only the energy difference for the conversion of LE to CT excitons, we consider the LE-CT couplings and analyze if the disorder in them could be indicative of some dimers not participating in the process. We also investigate if for such

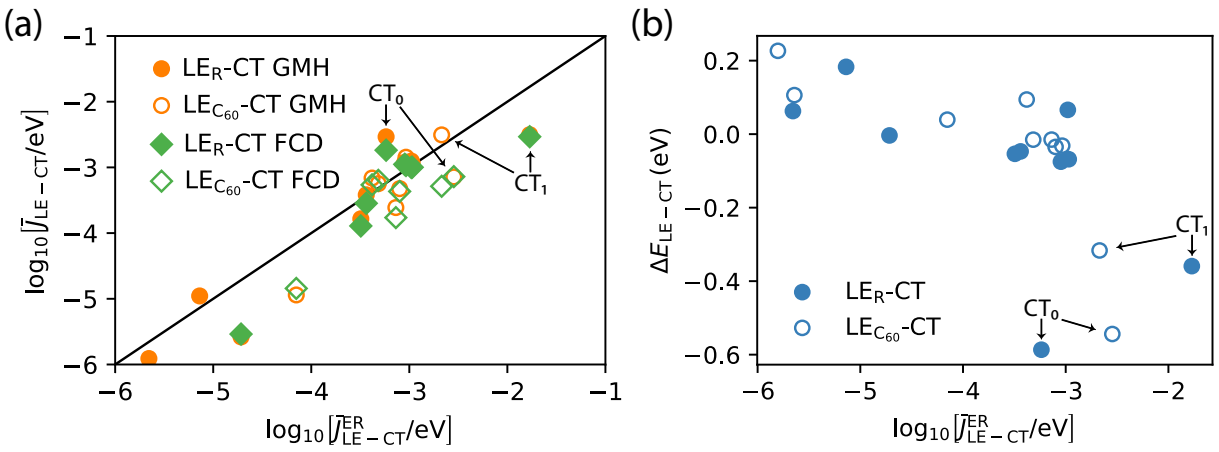

Figure 3: (a) Effective LE-CT couplings (see Eq. (40)) in the rubrene-C_{60} dimers resulting from polarizable *GW*-BSE/MM calculations with the GMH and FCD diabatization schemes against those from ER. (b) Relation between LE-CT energy difference $\Delta E_{\text{LE-CT}} = \Omega_{\text{CT}} - \Omega_{\text{LE}}$ and the LE-CT coupling from *GW*-BSE ER diabatization.

large bi-molecular structures, the use of GHM, FCD, and ER diabatization has any influence on the results.

A specific aspect of the rubrene-C_{60} systems that requires extra is the (near) degeneracy of the 15 lowest LE on C_{60}, stemming from the 5-fold degeneracy of its HOMO and 3-fold degeneracy of its LUMO. For the same reason, also the CT states are 3-fold near degenerate. We take this into account by calculating an *effective* diabatic coupling[43,44] between N_{LE}-fold degenerate LEs and N_{CT}-fold degenerate CT excitons as

$$\bar{J}_{\text{LE}_x-\text{CT}} = \sqrt{\frac{\sum_{m=1}^{N_{\text{LE}}} \sum_{n=1}^{N_{\text{CT}}} J^2_{\text{LE}_{x,m}-\text{CT}_m}}{N_{\text{LE}} \cdot N_{\text{CT}}}}, \tag{40}$$

with $J_{\text{LE}_{x,m}-\text{CT}_n}$ the coupling element between the m-th degenerate LE and the n-th degenerate CT. The results from the different diabatization methods are shown in Fig. 3(a). There, we plot the couplings obtained with GMH and FCD diabatization against those from ER, and distinguish between LE$_R$-CT (filled symbols) and LE$_{C_{60}}$-CT (open symbols) couplings. Roughly speaking, the effective couplings from ER cover a range from 0.02 meV to 17 meV, with many occurring close to 1 meV. Compared to the small-molecule naphthalene-TCNE

dimer with ideal stacking, we find a stronger dependence on the diabatization method, although the differences between GMH and FCD seem minor in most cases. Of particular interest are the couplings of the two low-energy CT states, CT_0 and CT_1, as marked in Fig. 3(a). Specifically, the LE_R-CT couplings are different using ER (0.6 meV vs. 17 meV), while similar when using GMH at about 3 meV. As the ER method takes the full details of the electronic (transition) densities into account, it stands to reason that the extra details have a bigger contribution to the LE-CT couplings for more disordered structures and larger molecular building blocks.

In Fig. 3(b) we show the relation between the energy offset of LE and CT states, calculated as $\Delta E_{\text{LE-CT}} = \Omega_{\text{CT}} - \Omega_{\text{LE}}$, and the LE-CT couplings obtained with ER. From Eq. (27) one generally expects some dependence of the couplings on the energy difference. Some dependence is visible in Fig. 3(b), although it is hard to ascribe a definite trend to the data. Noteworthy is that the two dimers with the most negative energy offsets corresponding to the two low energy CT states discussed in Section 3.2.1. In particular, CT_1 at energy 1.65 eV is found to have the highest coupling between the rubrene LE and the CT state. In comparison, the coupling to the lowest CT state, CT_0, is smaller by a factor of 30. This raises the question what impact the differences in couplings have for the LE-CT conversion dynamics, particularly which of the CT states is most likely to be probed over which timescale.

3.2.3 Kinetic Model

To scrutinize the effects of the disorder in energies and LE-CT couplings obtained from the *GW*-BSE/MM calculations in Sections 3.2.1 and 3.2.2 and the influence of different diabatization methods, we now study the conversion dynamics between LE and CT excitations with a kinetic model based on Marcus rates as in Eq. (1). This model requires in addition to the calculation of the LE-CT couplings and the excitation energies Ω also the determination of the respective reorganization energies λ_{ab}. Within the Marcus picture, $\lambda_{\text{LE}_x-\text{CT}} = E_{\text{CT}}(\text{LE}_x) - E_{\text{CT}}(\text{CT})$ and $\lambda_{\text{CT}-\text{LE}_x} = E_{\text{LE}_x}(\text{CT}) - E_{\text{LE}_x}(\text{LE}_x)$, where $x = \text{R},\text{C}_{60}$

and $E_a(G)$ represents the total energy of state a at geometry of state G. As such, this would require the cumbersome optimization of the dimer structures in the respective CT and LR states. Instead, we approximate the energies from monomer calculations, such that

$$E_{\mathrm{CT}}(\mathrm{LE_R}) = E_R^+(R^*) + E_{\mathrm{C_{60}}}^-(\mathrm{C_{60}^0}) \tag{41}$$

$$E_{\mathrm{CT}}(\mathrm{LE_{C_{60}}}) = E_R^+(R^0) + E_{\mathrm{C_{60}}}^-(\mathrm{C_{60}^*}) \tag{42}$$

$$E_{\mathrm{LE_R}}(\mathrm{CT}) = E_R^*(R^+) + E_{\mathrm{C_{60}}}^0(\mathrm{C_{60}^-}) \tag{43}$$

$$E_{\mathrm{LE_{C_{60}}}}(\mathrm{CT}) = E_R^0(R^+) + E_{\mathrm{C_{60}}}^*(\mathrm{C_{60}^-}) \tag{44}$$

$$E_{\mathrm{CT}}(\mathrm{CT}) = E_R^+(R^+) + E_{\mathrm{C_{60}}}^-(\mathrm{C_{60}^-}) \tag{45}$$

$$E_{\mathrm{LE_R}}(\mathrm{LE_R}) = E_R^*(R^*) + E_{\mathrm{C_{60}}}^0(\mathrm{C_{60}^0}) \tag{46}$$

$$E_{\mathrm{LE_{C_{60}}}}(\mathrm{LE_{C_{60}}}) = E_R^0(R^0) + E_{\mathrm{C_{60}}}^*(\mathrm{C_{60}^*}), \tag{47}$$

where the superscripts refer to the state of the monomers (0: ground state, +: cation, −: anion, ∗: excited). The total energy calculations and geometry optimizations in this step are performed using (time-dependent) DFT with the same basis set and functional as the *GW*-BSE calculations in Section 3.2.1, and we obtain $\lambda_{\mathrm{LE_R-CT}} = 0.12\,\mathrm{eV}$, $\lambda_{\mathrm{CT-LE_R}} = 0.12\,\mathrm{eV}$, $\lambda_{\mathrm{LE_{C_{60}}-CT}} = 0.18\,\mathrm{eV}$, and $\lambda_{\mathrm{CT-LE_{C_{60}}}} = 0.21\,\mathrm{eV}$, respectively. In similar spirit, we determine the vertical to adiabatic energy relaxations of the excited states, $\Lambda_a = E_a(0) - E_a(A)$, as $\Lambda_{\mathrm{CT}} = 0.15\,\mathrm{eV}$, $\Lambda_{\mathrm{LE_R}} = 0.16\,\mathrm{eV}$, and $\Lambda_{\mathrm{LE_{C_{60}}}} = 0.23\,\mathrm{eV}$.

With all energies and coupling elements at hand, we determine all rates between LE and CT states according to Eq. (1) at $T = 300\,\mathrm{K}$ for the kinetic model, which describes the time-evolution of the state population probabilities $\mathbf{P}(t)$ via a system of ordinary differential equations of the kind

$$\frac{d}{dt}\mathbf{P}(t) = \underline{\mathbf{W}}\mathbf{P}(t). \tag{48}$$

In this specific case, $\mathbf{P}^T(t) = [P_{\mathrm{LE_R}}(t), \mathbf{P}^T_{\mathrm{LE_{C_{60}}}}(t), \mathbf{P}^T_{\mathrm{CT}}(t)]$ is of dimension 21, and $\sum_i P_i(t) = 1$ for all t. The structure of the off-diagonal entries of the matrix $\underline{\mathbf{W}}$ is shown in Fig. 4,

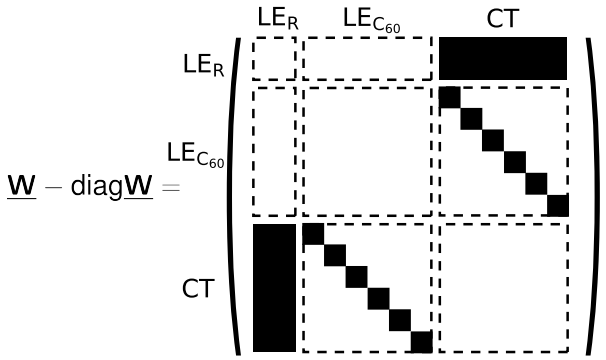

Figure 4: Schematic representation of the rate matrix of a kinetic model, with full squares indicating where the respective rates with LE-CT couplings occur.

emphasizing again that in this minimal model, we only consider transitions between LE and CT states, not between different LE, and different CTs. The diagonals of $\underline{\mathbf{W}}$ contain the negative of the sum of all other column entries, i.e., $W_{ii} = -\sum_j W_{ji}$.

We initially prepare the system in the $\mathrm{LE_R}$ state, i.e., $\mathbf{P}^T(t = 0) = [1, 0, \ldots, 0]$ and numerically study the evolution of Eq. (48) for $t_{\max} = 1\,\mu$s using the backward Euler scheme[45] with 10^5 steps. In Fig. 5(a), we show the resulting population probabilities with the LE-CT couplings calculated using ER diabatization. Initially, the population of the $\mathrm{LE_R}$ state decays rapidly and it is completely depopulated within 50 ps. This initial decay occurs primarily into three CT states, with a clear preference for the $\mathrm{CT_1}$ state. After 50 ps the two additionally populated CT states convert first into $\mathrm{LE_{C_{60}}}$ as intermediates in the timescale of 100 [ps] to 10 ns, until they also decay nearly exclusively into $\mathrm{CT_1}$. Note that we do not observe over the timescale of 1 μs a noticeable population of the lowest energy CT state, $\mathrm{CT_0}$. As can be seen from Fig. 5(b), there are some qualitative similarities when the dynamics are modeled based on GMH diabatization. In particular, the same rapid initial decay of $\mathrm{LE_R}$ and the final near complete population of $\mathrm{CT_1}$ can be seen. Some quantitative difference can be noted in the details of the intermediate dynamics. Initially, $\mathrm{CT_1}$ does not get populated. Instead, the populations of the two other CT states is much higher and, consequently, also the populations of the two intermediate $\mathrm{LE_{C_{60}}}$ they convert into.

We also report in Fig. 5(c) the expectation value of the measured CT energy, calculated

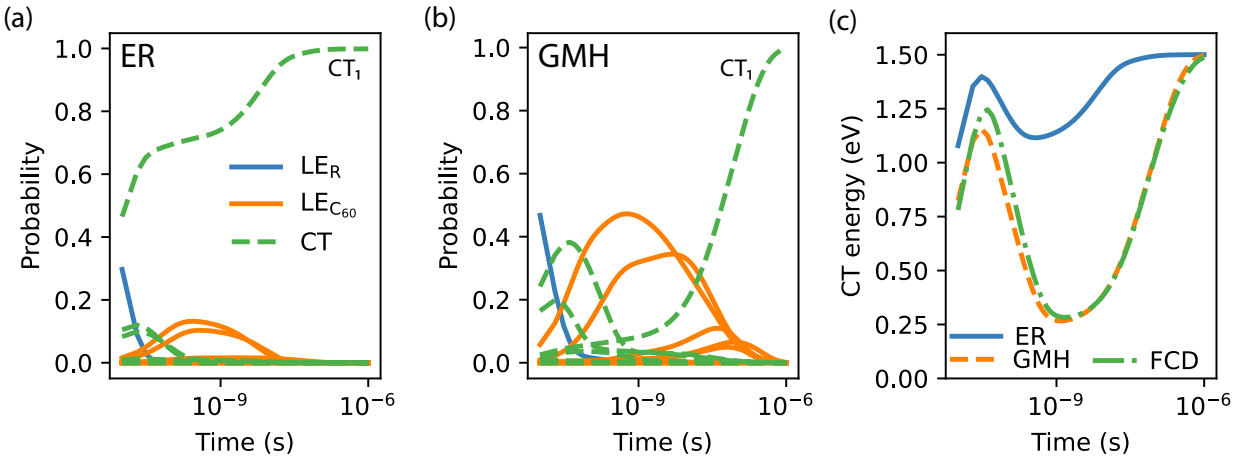

Figure 5: (a) Population dynamics of the excited states for $t_{\max} = 1\,\mu$s as a solution to Eq. (48) for LE-CT couplings from ER diabatization. The blue line indicates the population of the $\mathrm{LE_R}$ excited state, orange lines the ones of the respective $\mathrm{LE_{C_{60}}}$, and green dashed lines populations of CT states, respectively. (b) Same for GMH diabatization. (c) Time evolution of the expected CT energy $\langle\Omega_{\mathrm{CT}}\rangle$ from population probabilities based on models with different diabatization methods.

according to

$$\langle\Omega_{\mathrm{CT}}(t)\rangle = \sum_{n=1}^{10} P_{\mathrm{CT}_n}(t)\Omega_{\mathrm{CT}_n}, \tag{49}$$

for the three different diabatization methods considered in this work. As could be expected from the individual populations over time, the expected CT energy follows similar trends. At about 50 ps, all methods exhibit a peak, whose height depends slightly on the method. Its energy of more than 1 eV is, however, a consequence of the low population of high energy (~ 2 eV) CT states, and not indicative of the population of either $\mathrm{CT_0}$ or $\mathrm{CT_1}$. The dip following the peak is a combined effect of the depopulation of the high-energy CT states to both $\mathrm{CT_1}$ (in case of ER) and some $\mathrm{LE_{C_{60}}}$. In the model based on GMH/FCD, the cumulative population of all CT states is minimal at $t = 1$ ns, leading to the pronounced reduction of the expected CT state energy. On the other hand, in the ER model, the $\mathrm{CT_1}$ state is already populated at this time, but the combination of it being a low energy excitation and only partially populated (around 0.6) still leads to a smaller but noticeable minimum. Only on the timescale of $1\,\mu$s, when the $\mathrm{CT_1}$ population is nearly 1, $\langle\Omega_{\mathrm{CT}}(t)\rangle$ is indicative of a pure CT

state. Interestingly, the value of $\langle \Omega_{\mathrm{CT}}(t = 1\,\mu\mathrm{s}) \rangle = 1.50\,\mathrm{eV}$ is close to the CT energy reported in experiments (1.46 eV),[21] although we do not want to overstress this apparent agreement due to the limited nature of the model. Noteworthy in this context is also that in both cases (ER and GMH/FCD), no population of CT_0 is observed in the considered timescale. In thermal equilibrium ($t \to \infty$), one would expect the state occupation probabilities to be Boltzmann distributed according to

$$P_i^{\mathrm{th}} = \frac{\exp(-\beta\Omega_i)}{\sum_{i=1}^{21} \exp(-\beta\Omega_i)}, \tag{50}$$

and as such, an almost complete population of CT_0. While out limited model appears to run into a different equilibrium with complete CT_1 occupation as in Fig. 5, this is misleading, as even in the model a conversion to CT_0 will happen on a much longer timescale. Note, however, that adding additional conversion pathways to the model is expected to reduce the time in which the system reaches thermal equilibrium, but doing so is beyond the scope of this work which focuses on the analysis of different diabatization methods with respect to the calculation of LE-CT couplings.

4 Summary

In summary, we have developed the determination of LE-CT coupling elements withing the framework of *GW*-BSE. We have shown that in an ideal small-molecule dimer of naphthalene and TCNE, the quantitative estimates of these couplings are largely insensitive to methodological choices in the *GW* and BSE steps of the calculation, and only small differences are noted between the Edmiston–Ruedenberg, Generalized Mulliken–Hush, and Fragment Charge Difference diabatization formalisms, respectively. Compared to literature results for this model system on TD-DFT level, we could show that the difference found in the *GW*-BSE-based calculations can be attributed to different predictions of the adiabatic dimer energies entering the diabatization procedure, and not differences in the densities of the

excitations.

In larger-scale, disordered molecular complexes, such as the low-donor content rubrene-fullerene mixtures, the LE-CT couplings are found to be more sensitive to the choice of the diabatization formalism. While the two more approximate Generalized Mulliken–Hush and Fragment Charge Difference approaches yield couplings that are largely in agreement with each other, they differ from respective results based on the Edmiston–Ruedenberg approach, which takes full details of the excited state densities into account. To scrutinize the effect of the different predictions both qualitatively and quantitatively, we have employed the respective LE-CT couplings in a minimal kinetic model of the conversion from LE to CT states based on Marcus rates. From the obtained time evolution of state population probabilities, it is apparent that the dynamics are affected on an intermediate timescale, but not the final steady state prediction.

Funding information B.B. acknowledges support by the Innovational Research Incentives Scheme Vidi of the Netherlands Organisation for Scientific Research (NWO) with project number 723.016.002. Partial funding is also provided by NWO and the Netherlands eScience Center for funding through project number 027.017.G15, within the Joint CSER and eScience program for Energy Research (JCER 2017).

References

(1) Rühle, V.; Lukyanov, A.; May, F.; Schrader, M.; Vehoff, T.; Kirkpatrick, J.; Baumeier, B.; Andrienko, D. Microscopic Simulations of Charge Transport in Disordered Organic Semiconductors. *J. Chem. Theory Comput.* **2011**, *7*, 3335–3345.

(2) de Vries, X.; Friederich, P.; Wenzel, W.; Coehoorn, R.; Bobbert, P. A. Full Quantum Treatment of Charge Dynamics in Amorphous Molecular Semiconductors. *Phys. Rev. B* **2018**, *97*, 075203.

(3) Degitz, C.; Schmid, M.; May, F.; Pfister, J.; Auch, A.; Brütting, W.; Wenzel, W. From Molecule to Device: Prediction and Validation of the Optical Orientation of Iridium Phosphors in Organic Light-Emitting Diodes. *Chem. Mater.* **2023**, *35*, 295–303.

(4) Marcus, R. A. Electron Transfer Reactions in Chemistry. Theory and Experiment. *Rev. Mod. Phys.* **1993**, *65*, 599–610.

(5) Hutchison, G. R.; Ratner, M. A.; Marks, T. J. Hopping Transport in Conductive Heterocyclic Oligomers: Reorganization Energies and Substituent Effects. *J. Am. Chem. Soc.* **2005**, *127*, 2339–2350.

(6) D'Avino, G.; Muccioli, L.; Castet, F.; Poelking, C.; Andrienko, D.; Soos, Z. G.; Cornil, J.; Beljonne, D. Electrostatic Phenomena in Organic Semiconductors: Fundamentals and Implications for Photovoltaics. *Journal of Physics: Condensed Matter* **2016**, *28*, 433002.

(7) Wehner, J.; Brombacher, L.; Brown, J.; Junghans, C.; Çaylak, O.; Khalak, Y.; Madhikar, P.; Tirimbò, G.; Baumeier, B. Electronic Excitations in Complex Molecular Environments: Many-Body Green's Functions Theory in VOTCA-XTP. *J. Chem. Theory Comput.* **2018**, *14*, 6253–6268.

(8) Tirimbò, G.; Sundaram, V.; Çaylak, O.; Scharpach, W.; Sijen, J.; Junghans, C.; Brown, J.; Ruiz, F. Z.; Renaud, N.; Wehner, J.; Baumeier, B. Excited-State Electronic Structure of Molecules Using Many-Body Green's Functions: Quasiparticles and Electron–Hole Excitations with VOTCA-XTP. *The Journal of Chemical Physics* **2020**, *152*, 114103.

(9) Onida, G.; Reining, L.; Rubio, A. Electronic Excitations: Density-Functional versus Many-Body Green's-Function Approaches. *Rev. Mod. Phys.* **2002**, *74*, 601–659.

(10) Baumeier, B.; Andrienko, D.; Ma, Y.; Rohlfing, M. Excited States of Dicyanovinyl-

Substituted Oligothiophenes from Many-Body Green's Functions Theory. *J. Chem. Theory Comput.* **2012**, *8*, 997–1002.

(11) Förster, A.; Visscher, L. Quasiparticle Self-Consistent GW-Bethe–Salpeter Equation Calculations for Large Chromophoric Systems. *J. Chem. Theory Comput.* **2022**, *18*, 6779–6793.

(12) Blase, X.; Attaccalite, C. Charge-Transfer Excitations in Molecular Donor-Acceptor Complexes within the Many-Body Bethe-Salpeter Approach. *Appl. Phys. Lett.* **2011**, *99*, 171909.

(13) Baumeier, B.; Andrienko, D.; Rohlfing, M. Frenkel and Charge-Transfer Excitations in Donor–Acceptor Complexes from Many-Body Green's Functions Theory. *J. Chem. Theory Comput.* **2012**, *8*, 2790–2795.

(14) Sharifzadeh, S.; Darancet, P.; Kronik, L.; Neaton, J. B. Low-Energy Charge-Transfer Excitons in Organic Solids from First-Principles: The Case of Pentacene. *J. Phys. Chem. Lett.* **2013**, *4*, 2197–2201.

(15) Baumeier, B.; Rohlfing, M.; Andrienko, D. Electronic Excitations in Push–Pull Oligomers and Their Complexes with Fullerene from Many-Body Green's Functions Theory with Polarizable Embedding. *J. Chem. Theory. Comput.* **2014**, *10*, 3104–3110.

(16) Duchemin, I.; Guido, C. A.; Jacquemin, D.; Blase, X. The Bethe–Salpeter Formalism with Polarisable Continuum Embedding: Reconciling Linear-Response and State-Specific Features. *Chem. Sci.* **2018**, *9*, 4430–4443.

(17) Edmiston, C.; Ruedenberg, K. Localized Atomic and Molecular Orbitals. *Rev. Mod. Phys.* **1963**, *35*, 457–464.

(18) Cave, R. J.; Newton, M. D. Generalization of the Mulliken-Hush Treatment for the

Calculation of Electron Transfer Matrix Elements. *Chemical Physics Letters* **1996**, *249*, 15–19.

(19) Hush, N. S. Adiabatic Theory of Outer Sphere Electron-Transfer Reactions in Solution. *Trans. Faraday Soc.* **1961**, *57*, 557–580.

(20) Mao, Y.; Montoya-Castillo, A.; Markland, T. E. Excited State Diabatization on the Cheap Using DFT: Photoinduced Electron and Hole Transfer. *J. Chem. Phys.* **2020**, *153*, 244111.

(21) Collado-Fregoso, E.; Pugliese, S. N.; Wojcik, M.; Benduhn, J.; Bar-Or, E.; Perdigón Toro, L.; Hörmann, U.; Spoltore, D.; Vandewal, K.; Hodgkiss, J. M.; Neher, D. Energy-Gap Law for Photocurrent Generation in Fullerene-Based Organic Solar Cells: The Case of Low-Donor-Content Blends. *J. Am. Chem. Soc.* **2019**, *141*, 2329–2341.

(22) Bechstedt, F. *Many-Body Approach to Electronic Excitations*, 1st ed.; Springer Series in Solid-State Science; Springer Berlin, Heidelberg, 2015.

(23) Hedin, L. New Method for Calculating the One-Particle Green's Function with Application to the Electron-Gas Problem. *Physical Review* **1965**, *139*, A796–A823.

(24) Hedin, L.; Lundqvist, S. In *Solid State Physics*; Seitz, F., Turnbull, D., Ehrenreich, H., Eds.; Academic Press, 1970; Vol. 23; pp 1–181.

(25) Hybertsen, M. S.; Louie, S. G. First-Principles Theory of Quasiparticles: Calculation of Band Gaps in Semiconductors and Insulators. *Physical Review Letters* **1985**, *55*, 1418–1421.

(26) Rohlfing, M.; Krüger, P.; Pollmann, J. Efficient Scheme for GW Quasiparticle Band-Structure Calculations with Applications to Bulk Si and to the Si(001)-(2x1) Surface. *Physical Review B* **1995**, *52*, 1905–1917.

(27) von der Linden, W.; Horsch, P. Precise Quasiparticle Energies and Hartree-Fock Bands of Semiconductors and Insulators. *Phys. Rev. B* **1988**, *37*, 8351–8362.

(28) Strinati, G. Application of the Green's Functions Method to the Study of the Optical Properties of Semiconductors. *La Rivista del Nuovo Cimento (1978-1999)* **1988**, *11*, 1–86.

(29) Golze, D.; Dvorak, M.; Rinke, P. The GW Compendium: A Practical Guide to Theoretical Photoemission Spectroscopy. *Front. Chem.* **2019**, *7*.

(30) Fetter, A. L.; Walecka, J. D. *Quantum Theory of Many-Particle Systems*; Dover Publications: Mineola, N.Y, 2003.

(31) Stone, A. J. Distributed Multipole Analysis: Stability for Large Basis Sets. *Journal of Chemical Theory and Computation* **2005**, *1*, 1128–1132.

(32) Subotnik, J. E.; Cave, R. J.; Steele, R. P.; Shenvi, N. The Initial and Final States of Electron and Energy Transfer Processes: Diabatization as Motivated by System-Solvent Interactions. *J. Chem. Phys.* **2009**, *130*, 234102.

(33) Cave, R. J.; Newton, M. D. Calculation of Electronic Coupling Matrix Elements for Ground and Excited State Electron Transfer Reactions: Comparison of the Generalized Mulliken–Hush and Block Diagonalization Methods. *J. Chem. Phys.* **1997**, *106*, 9213–9226.

(34) Neese, F. The ORCA Program System. *WIREs Computational Molecular Science* **2012**, *2*, 73–78.

(35) Adamo, C.; Barone, V. Toward Reliable Density Functional Methods without Adjustable Parameters: The PBE0 Model. *J. Chem. Phys.* **1999**, *110*, 6158–6170.

(36) Weigend, F.; Ahlrichs, R. Balanced Basis Sets of Split Valence, Triple Zeta Valence

and Quadruple Zeta Valence Quality for H to Rn: Design and Assessment of Accuracy. *Phys. Chem. Chem. Phys.* **2005**, *7*, 3297–3305.

(37) Weigend, F.; Häser, M.; Patzelt, H.; Ahlrichs, R. RI-MP2: Optimized Auxiliary Basis Sets and Demonstration of Efficiency. *Chemical Physics Letters* **1998**, *294*, 143–152.

(38) Chai, J.-D.; Head-Gordon, M. Long-Range Corrected Hybrid Density Functionals with Damped Atom–Atom Dispersion Corrections. *Phys. Chem. Chem. Phys.* **2008**, *10*, 6615–6620.

(39) Hutter, J.; Iannuzzi, M.; Schiffmann, F.; VandeVondele, J. Cp2k: Atomistic Simulations of Condensed Matter Systems. *WIREs Computational Molecular Science* **2014**, *4*, 15–25.

(40) Martínez, L.; Andrade, R.; Birgin, E. G.; Martínez, J. M. PACKMOL: A package for building initial configurations for molecular dynamics simulations. *Journal of Computational Chemistry* **2009**, *30*, 2157–2164.

(41) Bussi, G.; Donadio, D.; Parrinello, M. Canonical Sampling through Velocity Rescaling. *J. Chem. Phys.* **2007**, *126*, 014101.

(42) Bussi, G.; Zykova-Timan, T.; Parrinello, M. Isothermal-Isobaric Molecular Dynamics Using Stochastic Velocity Rescaling. *J. Chem. Phys.* **2009**, *130*, 074101.

(43) Newton, M. D. Quantum Chemical Probes of Electron-Transfer Kinetics: The Nature of Donor-Acceptor Interactions. *Chem. Rev.* **1991**, *91*, 767–792.

(44) Kirkpatrick, J. An Approximate Method for Calculating Transfer Integrals Based on the ZINDO Hamiltonian. *International Journal of Quantum Chemistry* **2008**, *108*, 51–56.

(45) Butcher, J. *Numerical Methods for Ordinary Differential Equations*, second edition ed.; John Wiley & Sons Inc: New York, 2008.